Retrieving clear-sky atmospheric parameters from SEVIRI and ABI infrared radiances

Xin Jin,[1] Jun Li,[1] Timothy J. Schmit,[2] Jinlong Li,[1] Mitchell D. Goldberg,[2] and James J. Gurka[3]

Received 28 February 2008; revised 16 May 2008; accepted 2 June 2008; published 15 August 2008.

[1] The algorithm for the current Geostationary Operational Environmental Satellite (GOES) Sounders is adapted to produce atmospheric temperature and moisture legacy profiles from simulated infrared radiances of the Advanced Baseline Imager (ABI) on board the next generation GOES-R. Since the Spinning Enhanced Visible and Infrared Imager (SEVIRI) on board the Meteosat Second Generation (MSG) Meteosat-8/9 has many of the same spectral and spatial features as ABI, it is used as proxy to test the algorithm. Because as imagers, SEVIRI and ABI do not have enough CO_2 absorption spectral bands relative to the current GOES Sounders, the legacy profile algorithm for the current GOES Sounders needs to be modified. Both simulations and analysis with radiance measurements indicate that the single temperature-sensitive infrared band (13.4 μm) of SEVIRI cannot provide enough temperature profile information. However, SEVIRI's two H_2O absorption spectral bands (6.2 and 7.2 μm) are able to provide useful information on water vapor content above 700 hPa. Because of their high spatial (approximately 3 km for SEVIRI and 2 km for ABI IR bands) and high temporal (15 min full disk coverage) resolutions, SEVIRI and ABI will provide useful profile products with a quality similar to that from the current GOES Sounder prior to the availability of a hyperspectral IR sounding system in geostationary orbit.

Citation: Jin, X., J. Li, T. J. Schmit, J. Li, M. D. Goldberg, and J. J. Gurka (2008), Retrieving clear-sky atmospheric parameters from SEVIRI and ABI infrared radiances, *J. Geophys. Res.*, *113*, D15310, doi:10.1029/2008JD010040.

1. Introduction

[2] The current Geostationary Operational Environmental Satellite (GOES) Sounder [*Menzel and Purdom*, 1994; *Schmit et al.*, 2002] operational products include clear-sky radiances, atmospheric temperature and moisture profiles, total/layer precipitable water, cloud top pressure, and water vapor tracked winds. Applications of those products include: nowcasting and forecasting of weather events, assimilation of cloud products into regional numerical forecast models, and monitoring of temperature and moisture changes in the preconvective periods. Retrieval algorithms have been developed for GOES Sounder products [*Ma et al.*, 1999; *Li and Huang*, 1999; *Li et al.*, 2008], and products were validated [*Menzel et al.*, 1998; *Schmit et al.*, 2002]. The Advanced Baseline Imager (ABI) [*Schmit et al.*, 2005] on board the next generation of GOES satellite (GOES-R) has much finer spatial resolution (2 km for infrared bands) and much faster scan rate (15 min for full disk plus 5 min for CONUS plus 30 s for mesoscale regions). The ABI has the capability to scan a full disk scan in 5 min.

[3] However, as an imaging instrument, the ABI only has a few broadband infrared (IR) spectral bands that have atmospheric profile information, including one CO_2 absorption band (13.3 m), one O_3 absorption band and three H_2O absorbing bands (6.19, 6.95 and 7.34 μm). According to the weighting functions shown in Figure 1, the CO_2 band peaks at a height close to the surface and the three water vapor bands peak between the 700 and 300 hPa layers. The ABI brightness temperatures contain less information of the vertical distribution of temperature and humidity than the instruments with higher spectral resolution, such as Atmospheric Infrared Sounder (AIRS) [*Chahine et al.*, 2006] and Infrared Atmospheric Sounding Interferometer (IASI) [*Aires et al.*, 2002]. *Schmit et al.* [2008] have studied and concluded that ABI, when combined with forecast information, can continue the current GOES Sounder type products (atmospheric legacy profiles, cloud top properties, etc.) as an interim measure prior to the availability of a hyperspectral infrared sounding system in geostationary orbit. The pros and cons of ABI for continuation of the current sounder type products are analyzed. For example, the unique aspects of ABI legacy products are the high spatial resolution, the fast scan rate and full disk coverage, which is very important for mesoscale forecasts and nowcasting. This paper describes the algorithm used for clear-sky ABI

[1]Cooperative Institute for Meteorological Satellite Studies, University of Wisconsin–Madison, Madison, Wisconsin, USA.
[2]Center for Satellite Applications and Research, NESDIS, NOAA, Camp Springs, Maryland, USA.
[3]GOES-R Program Office, OSD, NESDIS, NOAA, Camp Springs, Maryland, USA.

Copyright 2008 by the American Geophysical Union.
0148-0227/08/2008JD010040

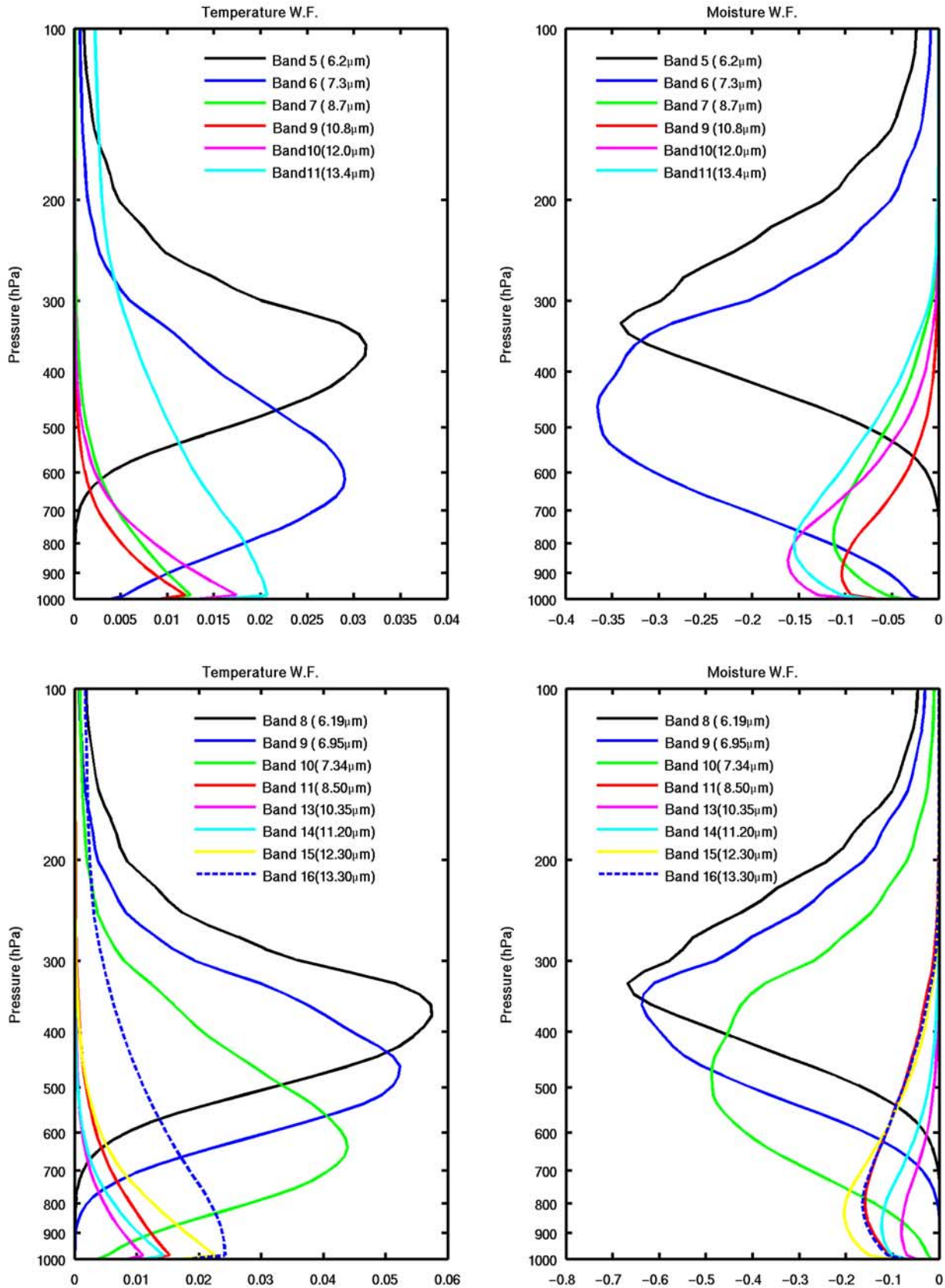

Figure 1. The weighting functions of (left) SEVIRI and (right) ABI IR bands calculated from the U.S. 1976 standard atmosphere at nadir view.

Table 1. Band Number and Wavelength of ABI and SEVIRI

ABI		SEVIRI	
Band	Wavelength (μm)	Band	Wavelength (μm)
1	0.47		
2	0.64	1	0.635
3	0.87	2	0.81
4	1.38		
5	1.61	3	1.64
6	2.25		
7	3.9	4	3.92
8	6.19	5	6.2
9	6.95		
10	7.34	6	7.35
11	8.5	7	8.7
12	9.61	8	9.66
13	10.35		
14	11.2	9	10.8
15	12.3	10	12
16	13.3	11	13.4

legacy profiles. Data from the Spinning Enhanced Visible and Infrared Imager (SEVIRI) on board the first Meteosat Second Generation (MSG) Meteosat-8/9 [*Schmetz et al.*, 2002] has been used as an ABI proxy in the algorithm development and evaluation.

[4] SEVIRI has similar spectral and spatial features to ABI (Table 1). As an imager, SEVIRI can finish a full disk scan within 15 min with a spatial resolution as high as 3 km (resampled). Figure 1 shows the temperature and water vapor (expressed as logarithm of mixing ratio) weighting functions (Jacobians) for SEVIRI (Figure 1, top) and ABI (Figure 1, bottom). SEVIRI only has one CO2 absorbing spectral band (13.4 μm) for air temperature retrieval and two H2O absorbing spectral bands (6.2 and 7.35 μm) for humidity retrieval. With one more H_2O absorption spectral band and better spatial resolution, ABI is expected to provide better moisture information than SEVIRI. To apply the legacy algorithm for SEVIRI and ABI, the current GOES Sounder algorithm needs to be modified.

[5] The operational algorithm for the GOES I-M Sounder uses the short-range forecast as a first guess and background in a nonlinear physical retrieval [*Ma et al.*, 1999]. Recently the algorithm was improved to include a regression as first guess [*Li et al.*, 2008] in CIMSS GOES Sounder routine processing. The improved retrieval system includes two components: a multivariable regression technique followed by a subsequent physical retrieval [*Li et al.*, 2000, 2008]. In this study, we tested both components by simulation and applied them to SEVIRI radiance measurements. However, the GOES Sounder algorithm was modified for SEVIRI: the regression coefficients for GOES Sounder are based on the collocated radiosondes, GOES Sounder radiances, and forecasts matchup data set, while the regression coefficients for SEVIRI/ABI are based on the synthetic radiances calculated from a near global training data set that contains temperature, moisture and ozone profiles, as well as surface skin temperature and surface IR emissivities [*Seemann et al.*, 2008]. Some useful profile-derived products such as the total precipitable water (TPW), the lifted index (LI), and the water vapor content at three significant layers (WV1: the water vapor content between surface and the 900 hPa layer; WV2: the water vapor content between 900 and 700 hPa layers; WV3: the water vapor content between 700 and 300 hPa layers) from SEVIRI are evaluated in this study because those are the current GOES Sounders' operational products. In addition, the impact of handling surface IR emissivities on the legacy profiles from SEVIRI/ABI radiances is studied.

[6] Our research is described in this paper as follows: in section 2, we present the data set for this study and briefly describe the algorithm. In section 3, a numerical simulation is applied to test the sensitivities of the algorithm to some additional factors, including surface emissivities and background errors. In section 4, a set of radiosonde (RAOB) profiles and a full disk case are selected to test the algorithm for application. Section 5 presents our concluding remarks.

2. Algorithms and Data Sets

2.1. Algorithm Description

[7] The improved GOES Sounder algorithm [*Li et al.*, 2008] uses the regression as the first guess (starting point of iteration in physical retrieval); the regression uses SEVIRI radiances and forecast as predictors. A global radiosonde data set with surface skin temperature and surface IR emissivities physically assigned [*Seemann et al.*, 2003, 2008] is used to generate the regression coefficient. The predictands include temperature and water vapor mixing ratio profiles; the basic predictors include SEVIRI/ABI IR spectral band brightness temperatures, surface pressure, land/ocean flag, and latitude. Since SEVIRI/ABI only has a few sounding spectral bands, the temperature/moisture profiles from short-range numerical weather prediction (NWP) forecast model are used as additional predictors in order to keep the vertical structure of forecast. The temperature forecast between 100 and 1013 hPa and mixing ratio forecast between 300 and 1013 hPa are used as additional predictors. Given $\boldsymbol{Y}$ (e.g., temperature or mixing ratio at a given pressure level) as a predictand, the regression equation is in the following format:

$$Z = A_0 + \sum_{j=1}^{N} B'_j Tb_j + \sum_{j=1}^{N} C'_j Tb_j^2 + \sum_{l=1}^{nt} b_{tl} T_l + \sum_{l=1}^{nw} b_{wl} \log(w_l) + D_1 p_s + D_2 \sec\theta + D_3 \cos(Lat), \quad (1)$$

here Tb is the brightness temperature; T(K) and w(g/kg) are forecast temperature and water vapor mixing ratio respectively; Ps(hPa), θ, and Lat are surface pressure, local zenith angle (LZA), and latitude, respectively. A, B, b, C and D are regression coefficients; N, nt and nw are the total number of SEVIR/ABI IR spectral bands, number of temperatures, and number of mixing ratios used as predictors. To derive the regression coefficients, a global data set containing temperature, moisture, and ozone profiles as well as the surface skin temperature, surface emissivities at SEVIRI and ABI IR spectral bands, are needed. We used a data set consisting of more than 15,700 global profiles of temperature, humidity and ozone [*Seemann et al.*, 2008]. A set of calculated BTs from a fast and accurate radiative transfer model is also required to generate the regression coefficients. The radiative transfer model applied here in simulating SEVIRI/ABI IR brightness temperatures is a fast transmittance model named Pressure-Layer Fast Algorithm for Atmospheric Transmittances (PFAAST) [*Hannon*

et al., 1996; *Eyre and Woolf*, 1988]. The fast transmittance model is built upon the transmittance profiles calculated by the line-by-line (LBL) radiative transfer model based on the high-resolution transmission molecular absorption spectroscopic database HITRAN 2000 [*Rothman et al.*, 1998]. The regression derived profile is used as the first guess for physical retrieval iterations. Since forecast profiles are used together with SEVIRI/ABI IR brightness temperatures as predictors, the regression should not be worse than the forecast if the BTs have good radiometric accuracy.

[8] In this study, we select six out of eight SEVIRI IR bands for predictors in the regression. We excluded the 3.9 μm band because it is negatively impacted by the solar radiation, showing a significant diurnal variation in BT, which is difficult to simulate in the training process. We also excluded the 8.7 μm band because it contains surface emissivity with large spatial variation over land and introduces high uncertainties for regression; however, the 8.7 μm band can be used over ocean. For the ABI simulations, the 3.9 and 8.5 μm bands are excluded for the same reasons. Of course the ABI will have additional bands that are not on the SEVIRI, such as three water vapor channels or a 10.35 μm band. Temperatures between 100 and 1013 hPa and mixing ratios between 300 and 1013 hPa from short-term numerical weather prediction (NWP) model forecasts are used as additional predictors in the regression.

[9] Once the regression retrieval is obtained, it is used as the first guess in the physical retrieval process. The physical approach uses an optimal method of combining observations with a background in the form of a forecast which is also used in the regression as additional predictors. In the physical retrieval, the 9.7 μm band is not used because it is strongly impacted by ozone uncertainty. The variational retrieval is performed by adjusting the atmospheric profile state, X, from the background, X^b, to minimize a cost function [*Rodgers*, 1976] of

$$J(X) = [Y^m - F(X)]^T E^{-1} [Y^m - F(X)] + \left[X - X^b\right]^T \gamma B^{-1} \left[X - X^b\right], \quad (2)$$

where **B** and **E** are the error covariance matrices of background, $\mathbf{X}^b$, and the observation (radiances) vector, $\mathbf{Y}^m$, respectively, **F**(**X**) is the forward radiative transfer model operator, γ is the regularization parameter (also called smoothing factor) which is introduced for convergence and solution stability. Superscripts T and -1 are the matrix transpose and inverse, respectively.

[10] By using the Newtonian iteration

$$X_{n+1} = X_n + J''(X_n)^{-1} \cdot J'(X_n), \quad (3)$$

the following quasi-nonlinear iterative form is obtained

$$\delta X_{n+1} = (F_n'^T \cdot E^{-1} \cdot F_n' + \gamma B^{-1})^{-1} \cdot F_n'^T \cdot E^{-1} \cdot \left(\delta Y_n + F_n' \cdot \delta X_n\right), \quad (4)$$

where **X** is the vector of temperature and humidity profile to be solved, **n** is the iteration step, **n** = 0 denotes first guess profile, $\delta X_n = X_n - X^b$, $\delta Y_n = Y^m - F(X_n)$, F' is the tangent linear operative (Jacobian) of forward model **F**. The regularization parameter is adjusted in each iteration according to the discrepancy principal [*Li and Huang*, 1999; *Li et al.*, 2000]. The reason to introduce the regularization parameter is to balance the contributions from the background and satellite observations in the solution, which is particularly important when the background (e.g., forecast) error is not Gaussian, or is only a locally Gaussian distribution.

[11] Since there are correlations among atmospheric variables, only a limited number of variables are needed to explain the vertical structure variation of an atmospheric profile [*Smith and Woolf*, 1976]. The number of independent structure functions can be obtained from a set of global atmospheric profile samples. Assume

$$X - X^b = \Phi A, \quad (5)$$

where $A = (\alpha_1, \alpha_2, \ldots, \alpha_M)$, and $\Phi = \begin{bmatrix} \Phi_T & 0 & 0 \\ 0 & \Phi_q & 0 \\ 0 & 0 & \Phi_{T_s} \end{bmatrix}$, Φ_T is the matrix of the first $\tilde{N}_T$ empirical orthogonal functions (EOFs) of the temperature profile, Φ_q is the matrix of the first $\tilde{N}_q$ EOFs of the water vapor mixing ratio profiles, $\Phi_{T_s} = 1$, and $M = \tilde{N}_T + \tilde{N}_4 + 1$. It is obvious that $\Phi^T \Phi = I$. Defining $\tilde{F}' = F' \cdot \Phi$, equation (4) becomes

$$A_{n+1} = \left(\tilde{F}_n'^T \cdot E^{-1} \cdot \tilde{F}_n' + \gamma B^{-1}\right)^{-1} \cdot \tilde{F}_n'^T \cdot E^{-1} \cdot \left(\delta Y_n + \tilde{F}_n \cdot A_n\right), \quad (6)$$

where $A_0 = 0$, and

$$\| F(A(\gamma) - Y^m) \|^2 = \sigma^2, \quad (7)$$

where σ is the observation error of SEVIRI [*Aminou et al.*, 2003], define $\|X\|^2 = \frac{1}{N}\sum_{i=1}^{N} x_i^2$, $X = (x_1, x_2, \ldots, x_N)$. Equation (5) and equation (6) are applied to derive the solution from SEVIRI radiances.

[12] For simulation purpose, we randomly selected 90% of the training data set to generate the regression coefficients, and applied the retrieval process to the remaining 10% of independent data set. In this study we had 1411 independent retrievals. There are three major aspects in the simulation are studied:

2.1.1. Error Covariance Matrix of the Background

[13] The background error estimate is based on the differences of temperature/moisture profiles between the rawinsonde data set and the spatially and temporally collocated National Centers for Environmental Prediction (NCEP) Global Forecast System (GFS) product which are used as the background in the GOES Sounder retrievals. In the training data set, the estimated errors are added to the true profile to simulate the forecast.

2.1.2. Surface IR Emissivities

[14] It is difficult to get the real surface IR emissivities at any time and for any location on the earth surface. The surface emissivities in the training data set are from operational MODIS emissivity products. In previous studies, the surface IR emissivities were set as constants with tiny random variations [*Seemann et al.*, 2003; *Li et al.*, 2000; *Zhou et al.*, 2002]. In this study, we take the IR emissivities as predictands in the training process, so that we can obtain

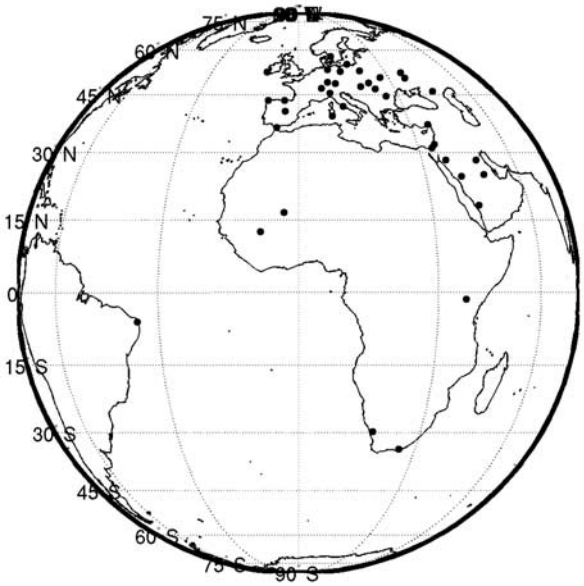

Figure 2. The radiosonde station map.

a group of estimated emissivities at SEVIRI spectral bands from the regression approach. These derived emissivities will be fixed during physical iterations.

2.1.3. Surface Skin Temperature

[15] The surface skin temperature is a key factor in radiative transfer model calculation. Surface skin temperature has large spatial and temporal variability. In the training data set, each profile is assigned with a surface skin temperature based on the relationship between surface air temperature and solar zenith and azimuth angles [*Seemann et al.*, 2003]. In the retrieval process, surface skin temperature is an unknown variable to be retrieved since no predetermined surface skin temperature observation can be used. Usually the error in surface skin temperatures from the NWF models is quite large, and the error covariance of background surface skin temperature should be set accordingly; for example, in previous studies [*Seemann et al.*, 2003; *Li et al.*, 2000; *Zhou et al.*, 2002], the surface skin temperature background is assumed to have a mean error of zero and a standard deviation of 10 K. In the SEVIRI physical retrieval, the surface skin temperature derived from regression is used as background as well as the first guess and is assumed an error of 2.5 K.

2.2. Data Set for SEVIRI Clear-Sky Physical Retrieval Study

[16] One month (August 2006) data sets are used for this study. These data sets include: SEVIRI full disk BTs at 3-km spatial resolution and 15-min temporal resolution; the full disk SEVIRI cloud mask products from the EUMETSAT agency at the same spatial/temporal resolution; the global radiosonde profiles collected at two standard moments: 0000 and 1200 UTC; the European Center for Medium range Weather Forecasting (ECMWF) 12-h forecast products for background; and the ECMWF 6-h analysis products as the truth for validation; Advanced Microwave Scanning Radiometer–EOS (AMSR-E) TPW products over ocean in August 2006 are prepared as independent validations.

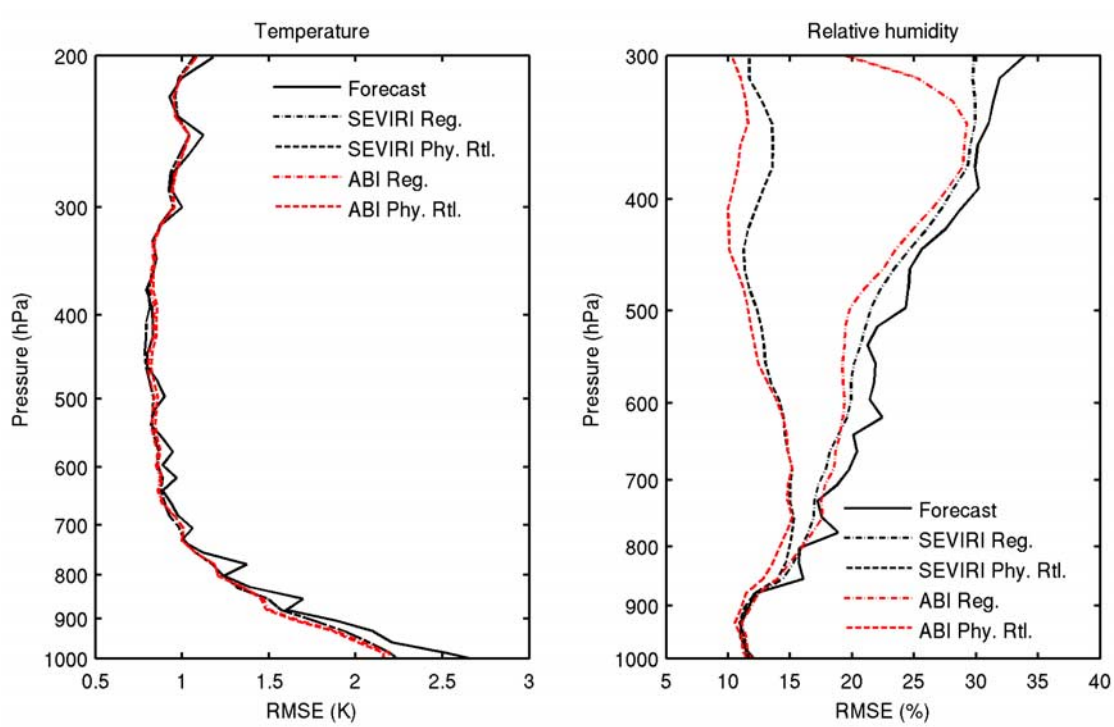

Figure 3. The simulated RMSE profiles of (left) temperature and (right) relative humidity. The solid line, black/red dash-dotted line, and black/red dashed line represent results from forecast, SEVIRI/ABI regression, and SEVIRI/ABI physical retrieval, respectively.

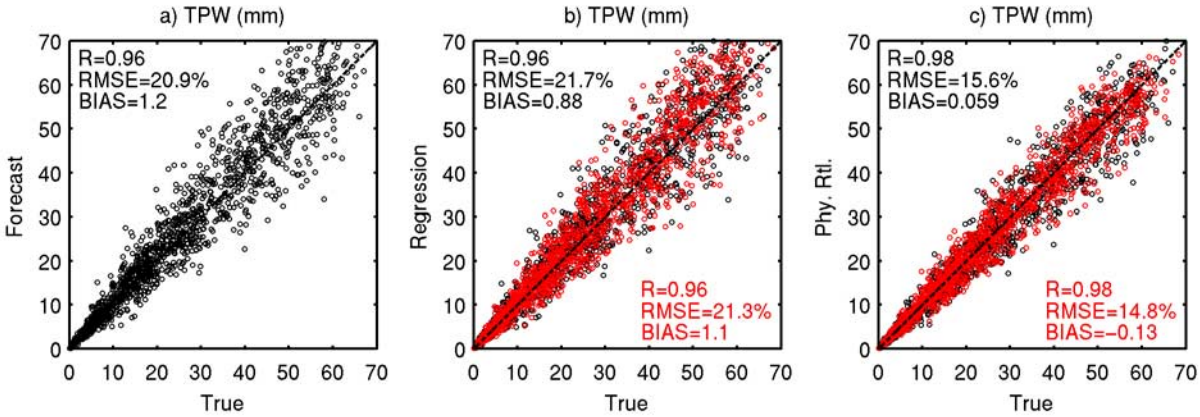

Figure 4. (a–c) The scattering plots of TPW (mm) between retrievals from simulation and truth. The dashed line in each panel is the 1-to-1 line. In Figures 4b (regression) and and 4c (physical), black and red plots represent results from SEVIRI and ABI, respectively.

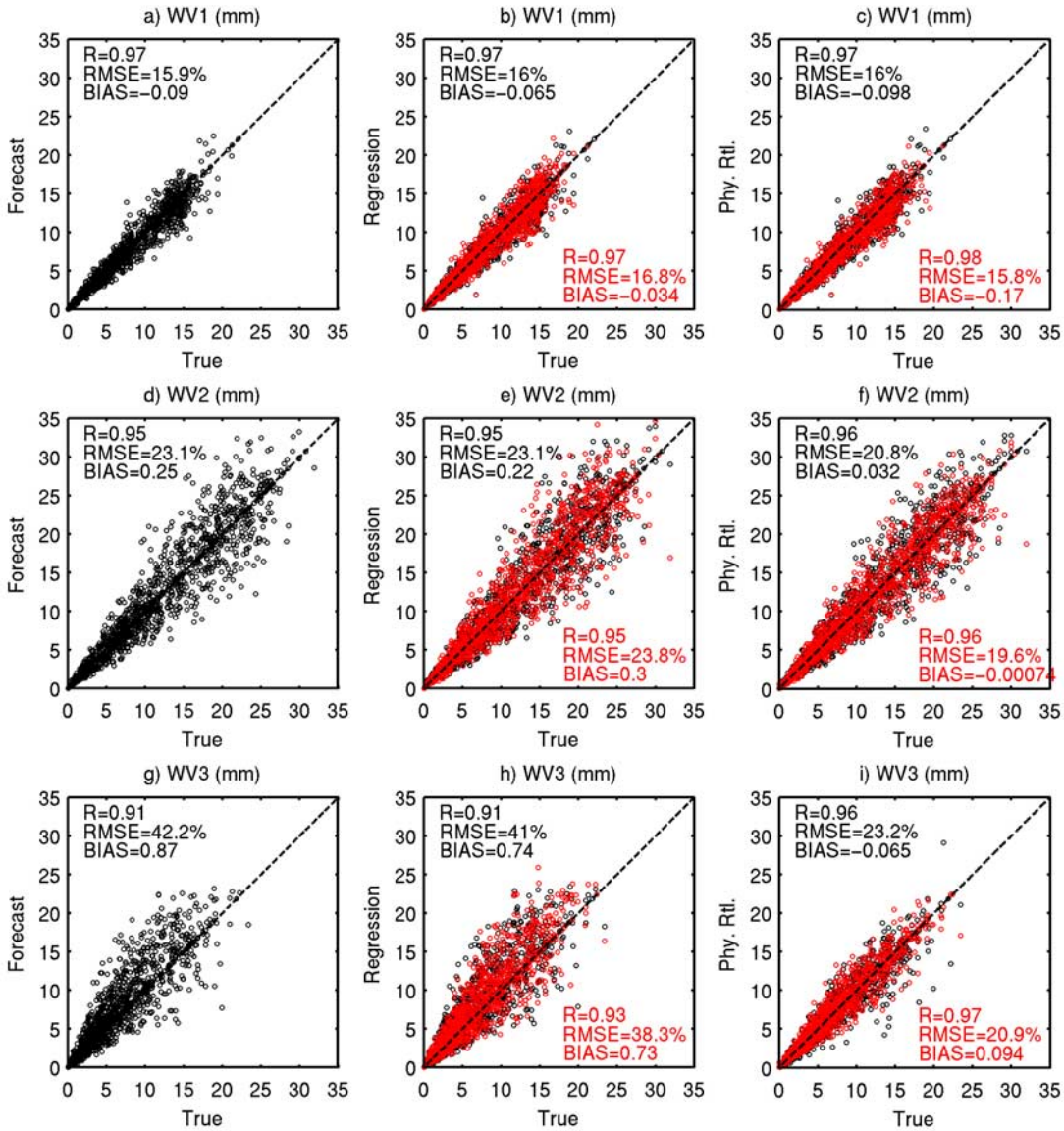

Figure 5. The simulated three water vapor components ((a–c) WV1, (d–f) WV2, and (g–i) WV3, all in mm) against the true. The dashed line in each panel is the 1-to-1 line. In Figures 5b, 5c, 5e, 5f, 5h, and 5i, black and red plots represent results from SEVIRI and ABI, respectively.

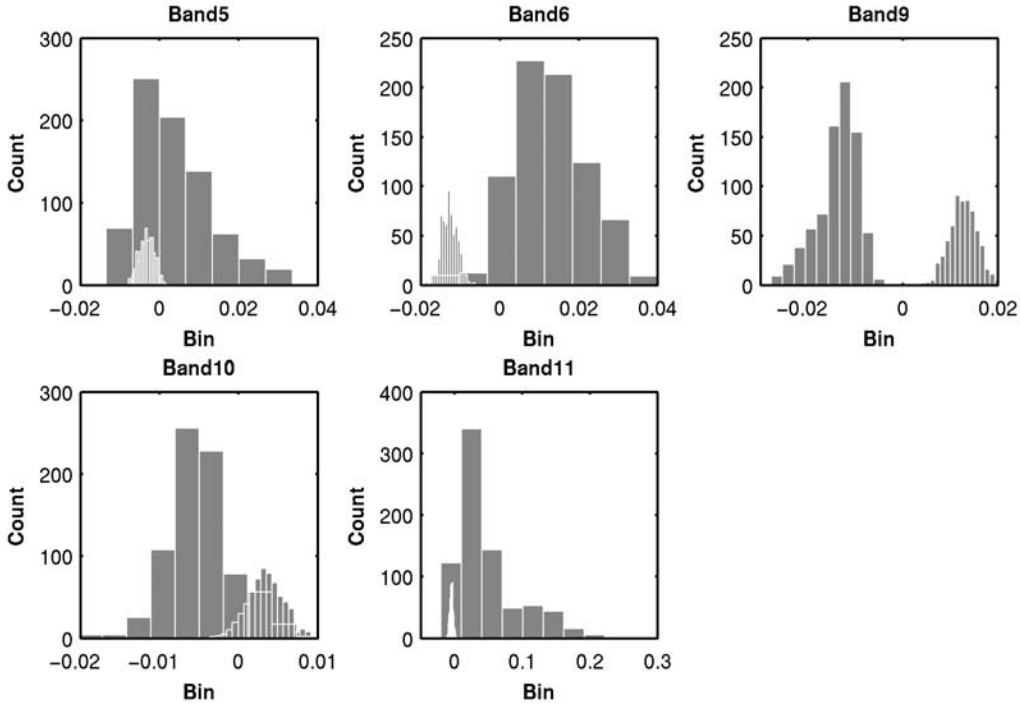

Figure 6. Histograms of the differences between regressed and true emissivities at five SEVIRI IR bands. In each panel, the thick bars represent 778 land cases, and the thin bars represent 633 oceanic cases.

[17] Assuming that each field of regard (FOR) contains 3 by 3 field of views (FOVs) or pixels, the clear-sky SEVIRI BTs within each FOV are averaged for parameter retrieval. The clear-sky pixels are selected on the basis of operational SEVIRI cloud mask products from EUMETSAT. The ECMWF products (both forecasts and analysis) have a 0.25×0.25 grid spatial resolution. A bilinear interpolation is performed spatially and temporally to get the closest profile for each SEVIRI pixel as the background (from forecast) or as the truth (from analysis). The ECMWF analysis profiles at the radiosonde sites and times (0000 UTC and 1200 UTC) are taken as the quality-controlled RAOBs for validation. A total of 365 RAOBs

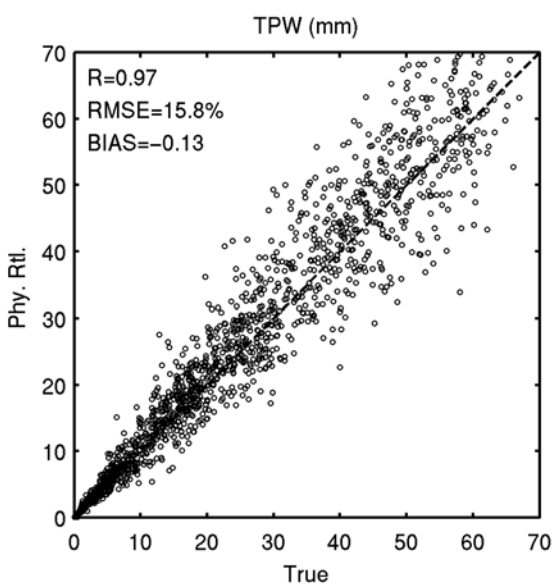

Figure 7. Same as Figure 4c but taking the true surface IR emissivities in calculation and only for SEVIRI simulation.

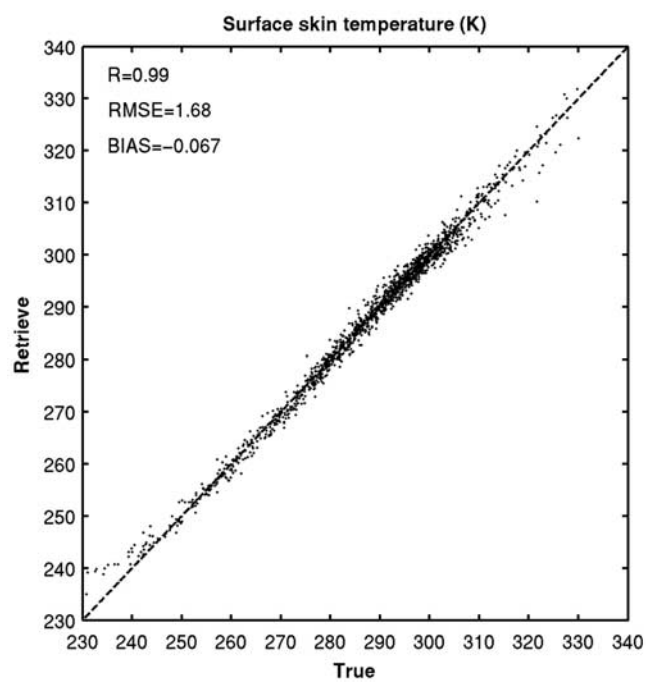

Figure 8. The regressed surface skin temperature against the true in the SEVIRI simulation. The dashed line is the 1-to-1 line.

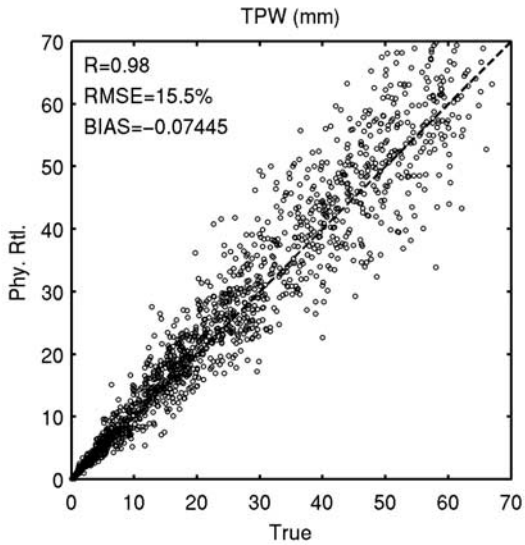

Figure 9. Same as Figure 4c but taking the true surface skin temperature in physical retrieval in SEVIRI simulation.

matching the SEVIRI observations under clear skies is obtained (Figure 2).

3. Simulation Studies

[18] In the simulation, retrieval of atmospheric temperature and moisture profiles along with the derived products, such as total precipitable water (TPW), lifted index (LI), WV1, WV2 and WV3, are compared with the truth. In

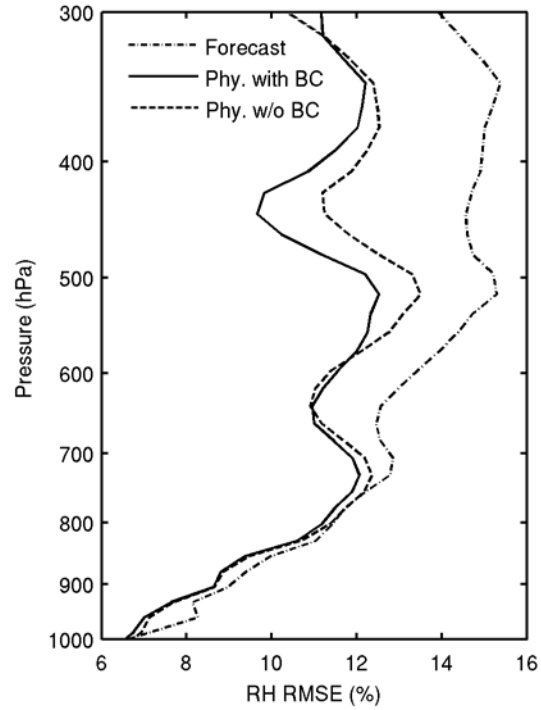

Figure 11. The retrieved RH RMSE profiles using SEVIRI brightness temperatures with (solid line) and without (dashed line) bias correction in physical retrieval. The dash-dotted line is the forecast RMSE for comparison.

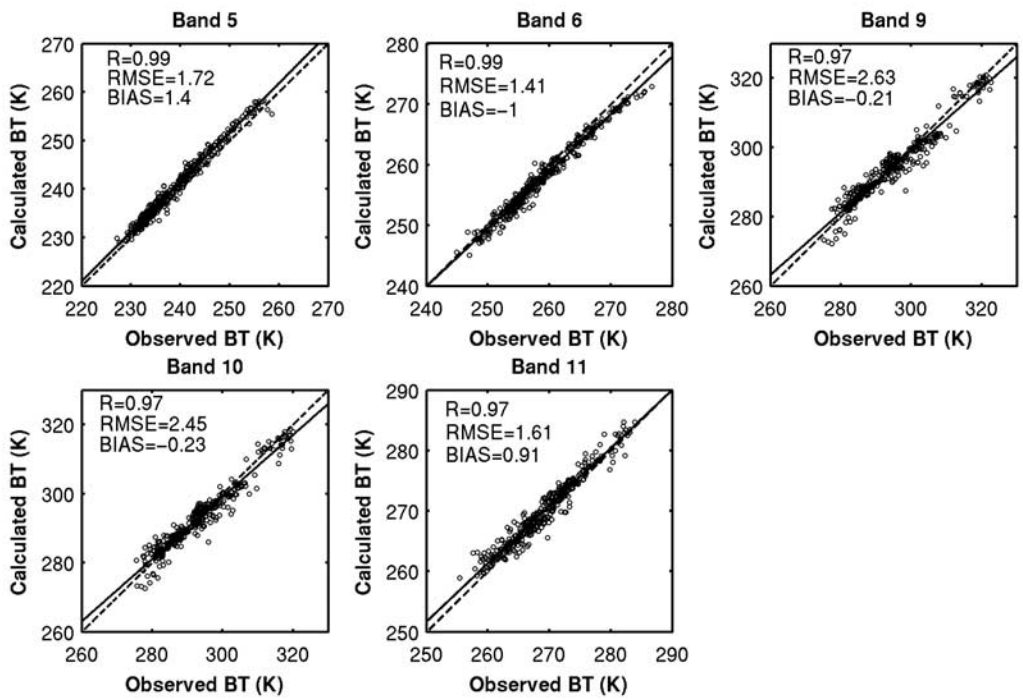

Figure 10. The comparison between the calculated and observed brightness temperatures at five IR bands for bias correction. In each panel the solid line represents the linear fitting, and the dashed line is the 1-to-1 line.

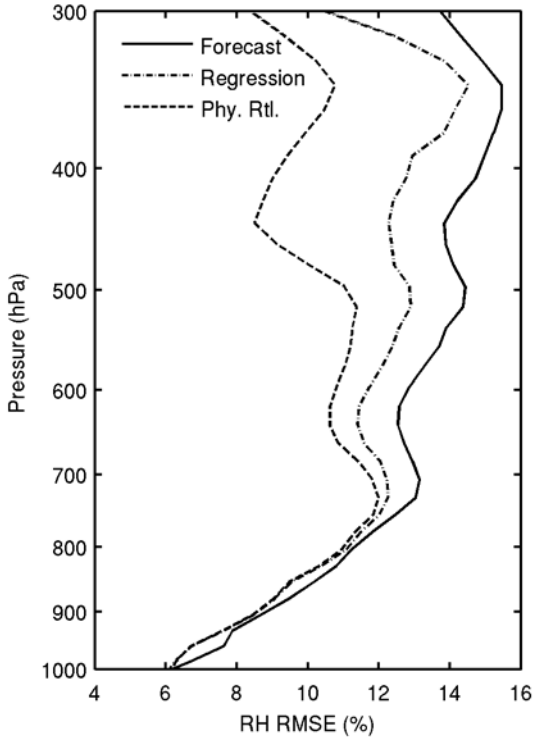

Figure 12. Same as Figure 3 but using RAOBs as true, ECMWF forecast as first guess for regression, and the difference between RAOBs and ECMWF forecast profiles as background.

addition, the impact of surface emissivity uncertainties on the clear-sky parameter retrievals is evaluated.

3.1. Profile Retrievals

[19] The root-mean-square errors (RMSE) of retrieved atmospheric temperature and moisture profiles from simulated SEVIRI/ABI radiances are shown in Figure 3. Moisture is represented by relative humidity (RH). The RMSE is based on the absolute differences between the retrievals and truth. For the temperature retrieval, neither the regression nor the physical retrievals substantially reduce the RMSE of the forecast that is taken as the background. This result is reasonable because there is only one CO_2 absorption spectral band on SEVIRI/ABI and there is not enough temperature profile information from this type of broad spectral satellite observation. However, for the humidity retrieval, the results are quite different. On the basis of the information contained in the two/three H_2O absorption spectral bands on SEVIRI/ABI, the RH RMSE between 700 and 300 hPa can be reduced by both approaches, which is consistent with the water vapor vertical information contained in the two/three H_2O absorption spectral bands (see Figure 1). Furthermore, the physical retrieval is much better than the regression because of the nonlinear solution of the radiative transfer model. In fact, the RH RMSE is almost locked between 10 and 15% at any pressure level by the physical retrieval. Although the window bands (8.7, 10.8, and 12.0 um) provide useful water vapor information near the surface, the RH RMSE under the 800 hPa layer is only slightly changed because of the difficulty in decoupling the impact of surface skin temperature in the physical retrieval [*Li*, 1994]. In addition, the ABI is better for retrieving moisture than SEVIRI because of one more H_2O absorption band.

3.2. Derived TPW Product

[20] The accuracy of TPW, derived from the profiles, is shown in Figure 4. Because of the significant improvement in RH RMSE, the TPW from the physical retrieval has a smaller RMSE against the truth when compared with the forecast. The improvement with the regression is almost undetectable because of the slight improvement in RH profile retrieval.

[21] When the profile is integrated into three parts (WV1, WV2 and WV3) the contribution of the water-vapor-absorbing bands on the moisture retrieval is clearly depicted. In Figure 5, the retrieved WV1 from both approaches has almost the same statistical features against the truth when compared with the forecast, indicating the weakness of SEVIRI/ABI in retrieving low-level water vapor content. For the retrieval of middle level water vapor, the regression method still does not show any decent improvement while the physical approach results in a noticeable improvement. The most significant improvement appears in the upper layers. Because of the humidity information provided by the water-vapor-absorbing bands, the physical retrieval reduces the WV3 RMSE from 42.2% to 23.2% for SEVIRI and 20.9% for ABI, respectively, while the regression method

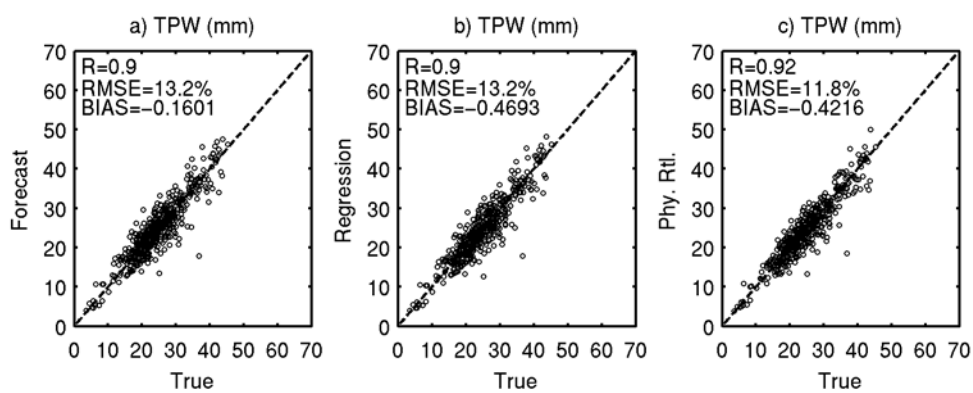

Figure 13. Same as Figure 4 but using RAOBs as true, ECMWF forecast as additional predictors in regression, and real SEVIRI observations for retrieval.

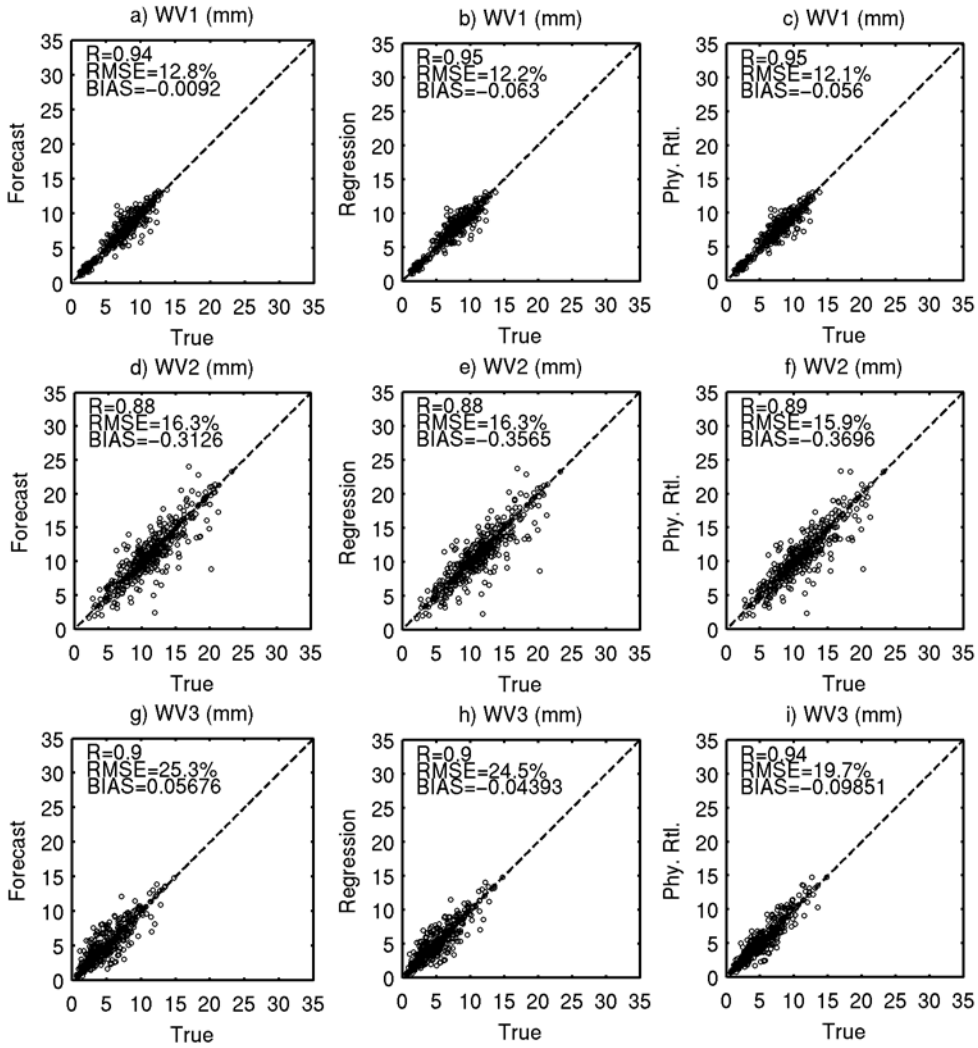

Figure 14. The three water vapor components (WV1, WV2 and WV3, all in mm) against truth (RAOBs). The dashed line in each panel is the 1-to-1 line. ECMWF forecast is used as additional predictors in regression.

only reduces the WV3 RMSE by 1% for SEVIRI and 4% for ABI against the forecast. Considering the weakness of the numerical model in predicting high-level water vapor, the WV3 product from the geostationary satellite imagers can significantly improve the model by providing upper level water vapor information at high spatial and temporal resolutions. In fact, ECMWF is assimilating the clear-sky water vapor radiances from a number of geostationary imagers [*Köpken et al.*, 2004; *Szyndel et al.*, 2005].

3.3. Impact of Surface IR Emissivities on Clear-Sky Parameters

[22] In the above numerical study, to make the simulation more realistic, the surface IR emissivities from the regression are used in the physical retrieval. The emissivity regression is based on the training data set that contains physically realistic IR emissivities assigned to each profile. Figure 6 shows the histogram of differences between the regressed emissivities and true values for 5 SEVIRI IR spectral bands. For oceanic cases, the variations in bias between the regressed and the true are quite small and for bands 5/9/10/11, almost all biases are within ±0.01. For land cases, the variations of bias are larger, but in general, most of the regressed emissivities are within ±0.02 relative to the true values.

[23] The regression determined emissivities are used in the physical retrieval, and the emissivities are fixed during the iterations. To check the impact of emissivity uncertainty on the physical retrieval, the ideal emissivities in physical retrieval is also attempted, for example, using the true emissivities in physical retrieval in the simulation. The results shown in Figure 7 indicate that the uncertainties in surface emissivities have a slight impact on the physical retrieval if 8.7 μm is not included. However, simulations might not fully reflect the real surface situation; for example, spatial and spectral variations of IR emissivity in 8.7 μm are quite large over desert region, which is difficult to simulate. The 8.7 μm band can be used over the ocean in the physical retrieval because of the uniform emissivity. Handling surface IR emissivities in the SEVIRI/ABI physical retrieval is important if all window bands are included, the possible approaches are (1) to use regression derived emissivities, which needs a realistic training; (2) to use predetermined

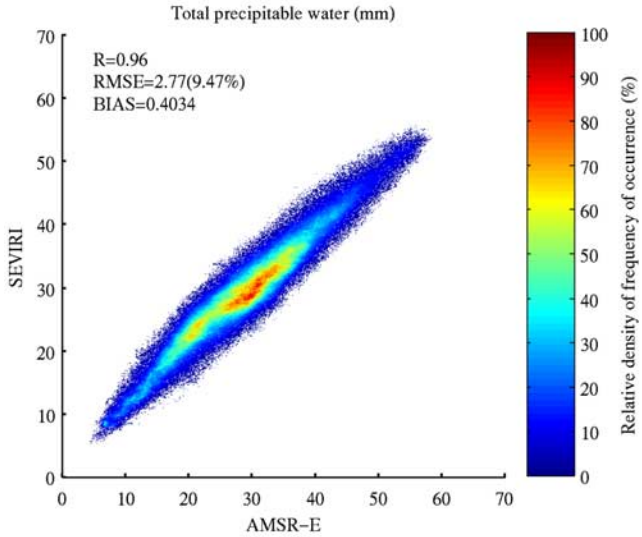

Figure 15. Density scattering plot of TPW between physical retrievals and AMSR-E over ocean in August 2006 (2,822,939 samples).

emissivity database, for example, from baseline fit database [*Seemann et al.*, 2008]; and (3) to use emissivity product from hyperspectral IR sounders on board polar orbiting satellites.

3.4. Impact by Surface Skin Temperature

[24] Another numerical experiment was designed to test the impact of surface skin temperature variation on the profile retrieval. Similar to the above emissivity testing, two configurations are tested: using the true skin temperature and regression derived skin temperature in physical iterations, respectively. Note that the surface skin temperature is fixed during the physical iterations if truth is used as both the background and the first guess, while the surface skin temperature is updated together with temperature and moisture profiles during physical iterations if regression skin temperature is used as first guess.

[25] The quality of the regressed skin temperature is checked before the experiment. As shown in Figure 8, in general the regressed surface skin temperatures have good agreement with the true temperatures. The bias is close to zero between 250 and 310 K, covering most possible surface situations within the SEVIRI full disk; the bias is negative when the skin temperature is higher than 310 K and positive when the skin temperature is lower than 250 K, the bias might be due to the inconsistent skin temperature assignment between 90% and 10% of data set in that temperature range.

[26] Results using the true skin temperature in the physical retrieval are shown in Figure 9. Relative to the impact caused by surface emissivity variation, the impact from surface skin temperature variation is larger. The correlation coefficient increases from 0.97 to 0.98 and the RMSE decreases 0.3%.

4. Application to SEVIRI Measurements

4.1. Bias Correction

[27] In this section, the algorithm is tested with quality-controlled radiosonde profiles collected at the stations shown in Figure 2. Before applying the algorithm, we make a radiance bias adjustment to minimize the uncertainty caused by the radiative transfer model or radiometric calibration. The results are shown in Figure 10. 365 collocated quality controlled RAOBs and SEVIRI radiance measurements are used. For band 5, the fitting line is almost parallel to the 1-to-1 line, illustrating a solid bias between calculations and observations at this band. For bands 6 and 11, a similar bias exists as well but not as significant as that for band 5. For the two "window" bands, i.e., bands 9 and 10, the bias is close to zero. According to the patterns in Figure 10, it is speculated that after the bias correction, the quality of the humidity profile may be improved, especially at the upper layer.

[28] As shown in Figure 11, because of the bias correction the RH RMSE profile is significantly improved, especially in the upper layers (between 600 and 300 hPa). The improvement in the lower levels (below the 700 hPa layer) also exists but not as pronounced as that in high levels; the improvement in the temperature profile retrieval is not shown here as it is too small. Since the bias is dependent in this study, improvement from bias adjustment is substantial; ideally an independent bias is needed for universal bias adjustment. A better bias estimate is very important for quality SEVIRI/ABI legacy profiles. In the following paragraphs, if not emphasized, the SEVIRI BTs used in the calculation are all bias corrected. One caveat of the bias correction maneuver is that all RAOBs are collected over land and the bias over ocean is still unknown.

4.2. Profile Retrievals

[29] The RMSE of RH profile retrievals is shown in Figure 12. In the retrieval, the ECMWF 12-h forecast profiles are used together with SEVIRI radiances in the regression, and the regressed profiles are used as the first guess in the physical retrieval. The forecast error profile is calculated by comparing the difference between RAOBs and ECMWF forecast profiles.

[30] The results with real data are similar to those in simulation. The improvement in the temperature RMSE profile is almost undetectable by both methods (not shown).

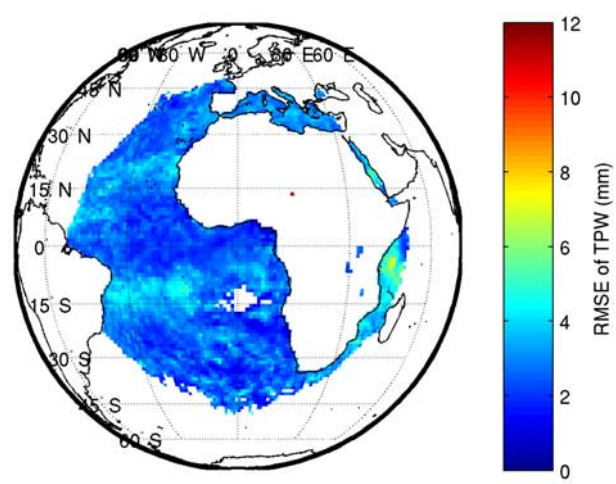

Figure 16. A full disk of RMSE between SEVIRI TPW and AMSR-E (pixels are grouped into each 1 × 1° boxes, and only boxes with more than 20 samples are considered).

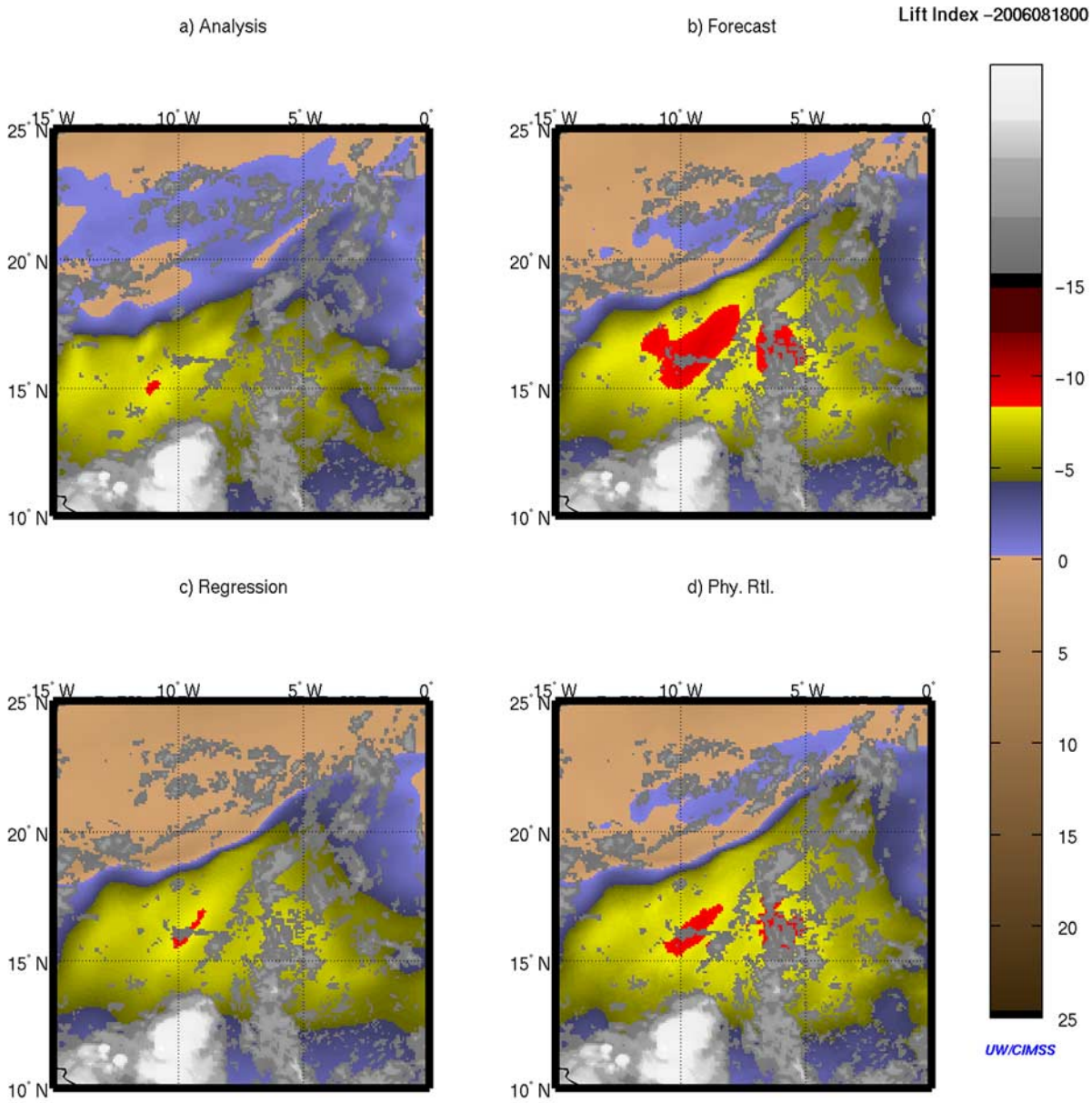

Figure 17. The lifted index derived from (a) ECMWF analysis, (b) ECMWF forecast, (c) regression, and (d) physical retrieval at 0000 UTC, 18 August 2006.

But the RH RMSE profile is solidly improved by both methods. After the physical retrieval, the RH RMSE profile is significantly improved between the 700 and 300 hPa layer. But for the profile lower than 800 hPa, the physical retrieval does not produce better results than the regression.

4.3. Derived Products

[31] The TPW from different methods are compared with that derived from RAOBs (Figure 13). The results are similar to the simulation in Figure 4. The regression shows almost no improvements in TPW. But after the physical retrieval, the TPW is noticeably better than the forecast. The three TPW components are also separated and compared with the ROABs (Figure 14). It is encouraging that both retrieval methods result in some improvement, even if only modest at times. For both methods, the greatest improvements are at lower pressure levels (e.g., higher altitudes). Although in a direct comparison, the physical retrieval shows better results than from the regression at lower pressure levels. For WV1, the RMSE derived from the physical approach shows only a 0.1% improvement over the regression which is 12.2% and the correlation coefficient R is improved from 0.90 to 0.92. For WV2, the RMSE from the physical method is 0.4% better, while for WV3, it is 4.8% better.

4.4. Comparison With AMSR-E

[32] AMSR-E TPW is a reliable product for independent validation with other satellite products [*Fetzer et al.*, 2006]. We have compared our retrieved TPW product with that from AMSR-E over the water. Because AMSR-E TPW has a spatial resolution of 20 km (compared to 9 km for SEVIRI

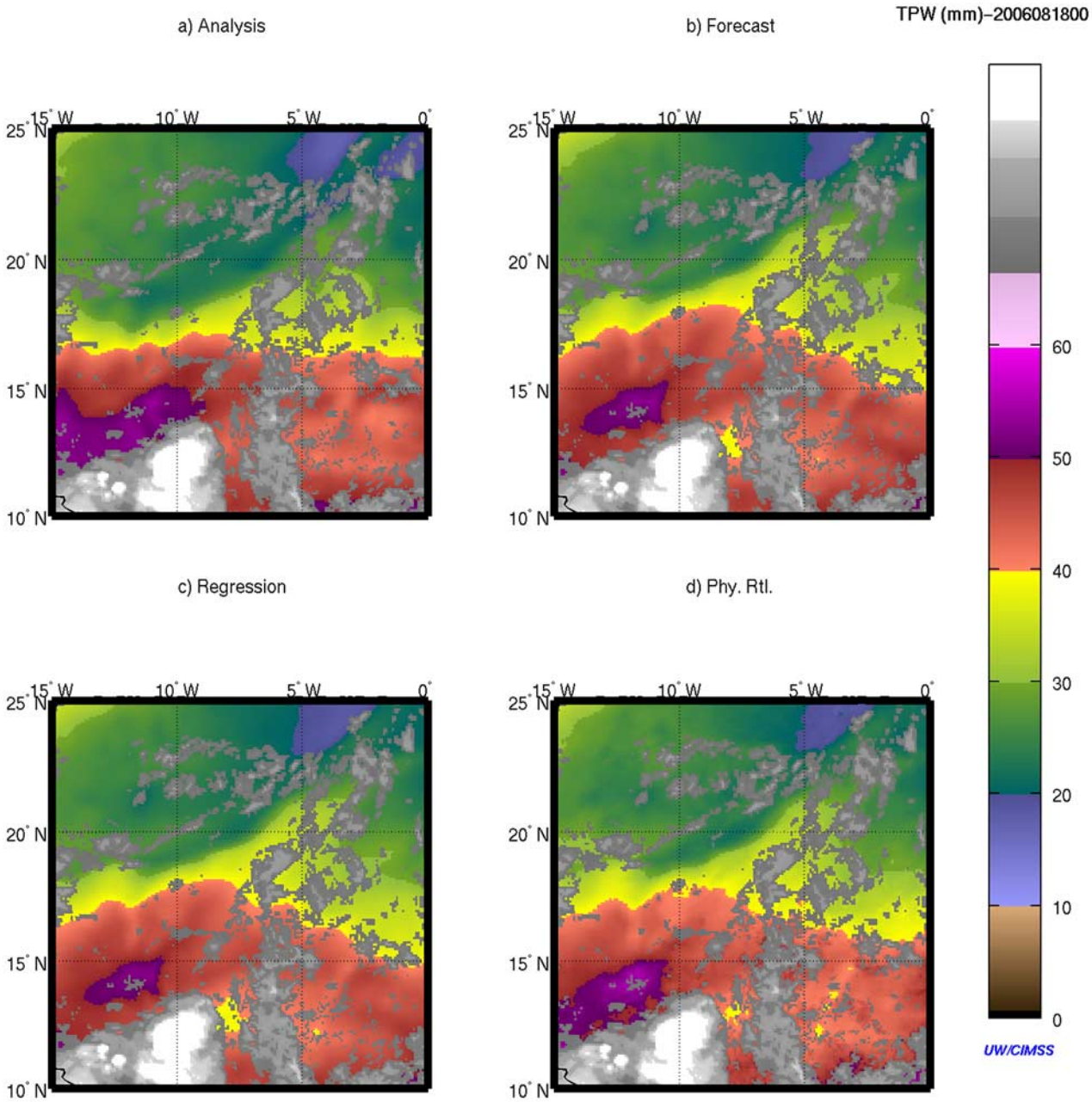

Figure 18. Same as Figure 17 but for TPW.

TPW), we only collect the SEVIRI pixels whose center is closer than 10 km to the AMSR-E pixel center. The collected SEVIRI TPW values are averaged to compare with the AMSR-E TPW; typically there are 4 SEVIRI records for each AMSR-E pixel. It should be noted that this operation inevitably smoothes the noise level of the SEVIRI TPW product. Concerning the temporal match, we take the moment of the AMSR-E crossing over the equator as reference, selecting the closest SEVIRI full disk for comparison. For the whole month (August 2006), there are more than two million qualified AMSR-E TPW records collected. The density scattering plot is shown in Figure 15. The correlation coefficient is 0.96 and the RMSE is smaller than 10%. For TPW measurements, this result is quite good. However, the SEVIRI TPW still shows some negative bias when the TPW is more than 25 mm and a positive bias when the TPW is less than 25 mm, as also reported by *Seemann et al.* [2003] using a similar algorithm and the MODIS BTs. Further studies are needed to investigate this issue. The spatial distribution of RMSE is presented in Figure 16. In most oceanic areas, the RMSE is smaller than 4 mm. In some areas of West Indian Ocean, the RMSE is as large as 7 mm. The only outlier appears in Chad Lake where the RMSE is close to 12 mm. As discussed earlier, the SEVIRI TPW is derived from IR radiances which are insensitive to surface emissivities. As a microwave instrument, it is very possible that the AMSR-E TPW is not as reliable here because of the impact of land surface emissiv-

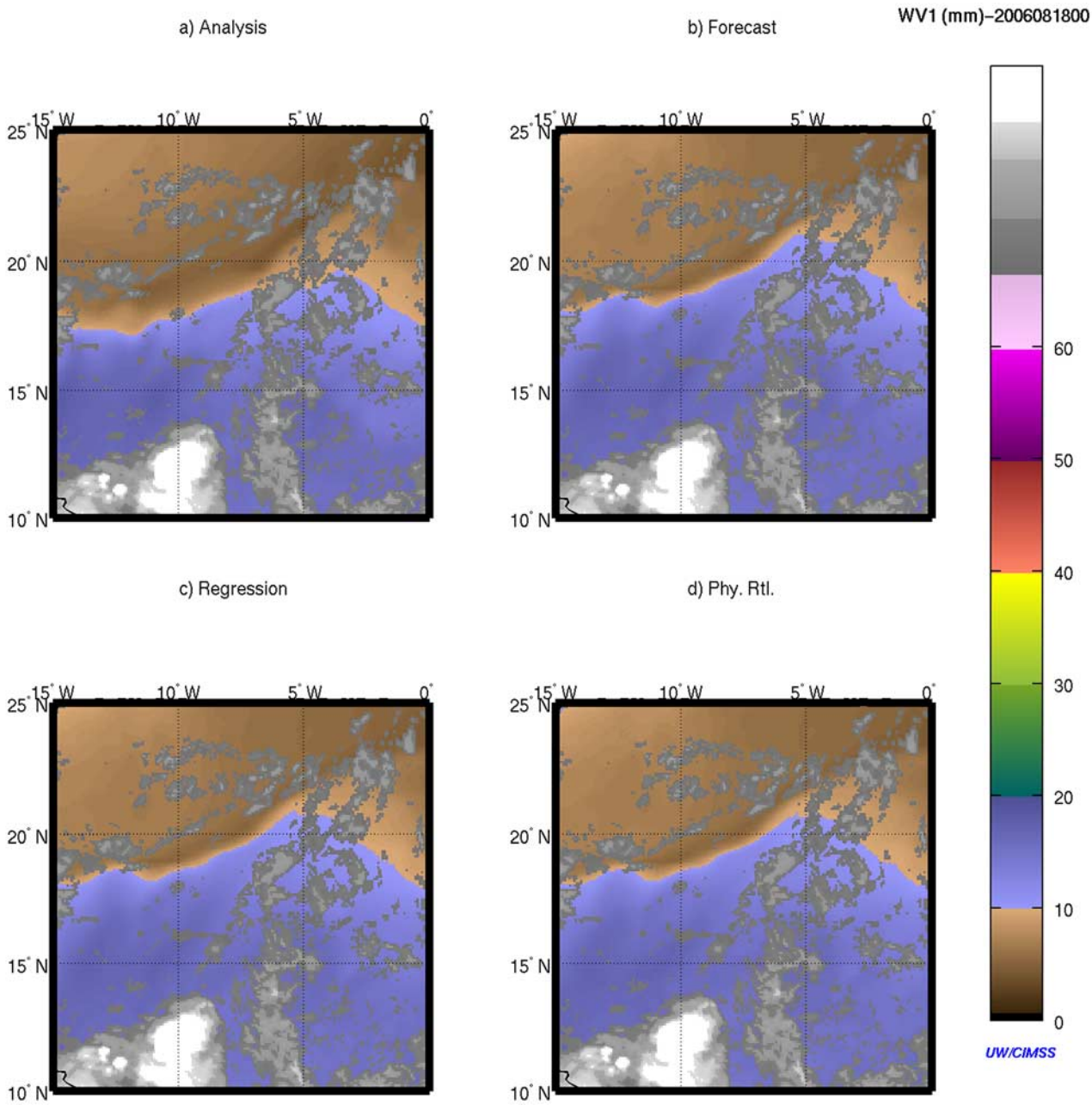

Figure 19. Same as Figure 17 but for WV1.

ity. Focusing on the pixels over the Atlantic Ocean and Mediterranean, they do not show noticeable variation with different local zenith angle (LZA).

4.5. Comparison With ECMWF Analysis Products

[33] A case at 0000 UTC on 18 August 2006 is selected to show the improvement in predicting severe weather with our retrieved atmospheric profiles. The LI, TPW, WV1, WV2 and WV3 are displayed in Figures 17–21, respectively. In Figure 17, the forecast model claims much larger areas of atmospheric instability than the actual conditions reported by the analysis. Both the regression and physical retrieval result in a better LI distribution than the forecast. The regression results in a minimal red area which seemingly makes it superior to the physical retrieval if only focusing on the red patches. However, as seen in the upper left part in each panel, the regression significantly underestimates the atmospheric instability, e.g., the LI in this area is larger than 0, indicating a stable atmospheric status while in other three panels, there are large blue patches indicating unstable areas. This pattern illustrates that with the regression the atmospheric status is biased to a more stable state; this result might be due to the fact that the profiles in the training data set are all collected in clear skies and therefore, in most cases, they represent a stable atmospheric status. The unstable conditions are not well regressed by the regression coefficients generated from such a data set. Comparing Figure 17b with Figure 17d, it is clear that the

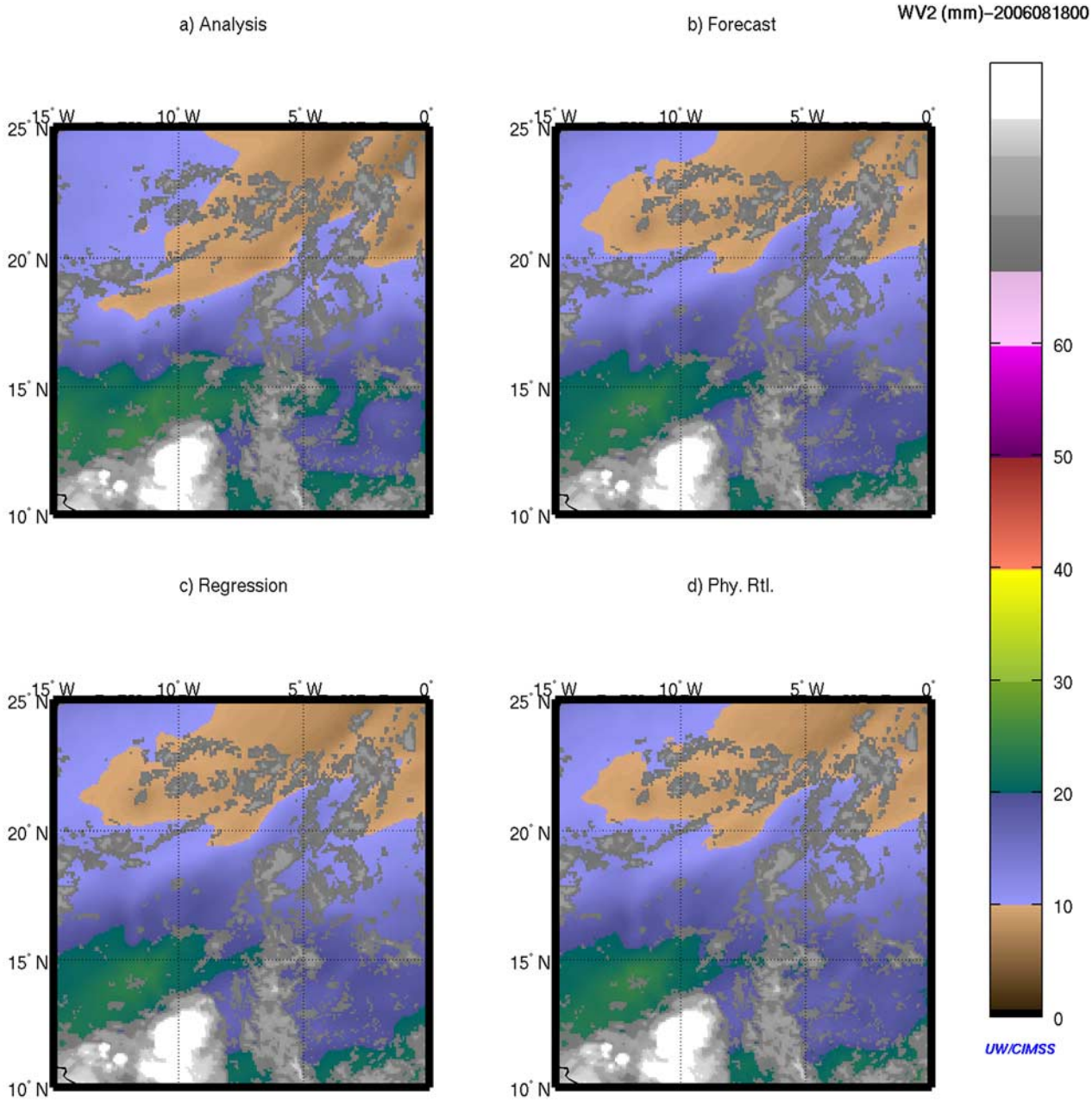

Figure 20. Same as Figure 17 but for WV2.

physical retrieval results in a better compromise. The area of red patches is significantly reduced and the blue patches in the upper left part are well represented.

[34] The images of TPW and its three components also illustrate the superiority of the physical retrieval to both the forecast and regression. In Figure 18, the purple area in the bottom left part of the panel indicates a very humid air mass (TPW > 50 mm). The forecast underestimates the size of this air mass and the regression does not provide any noticeable improvement in it. Only the physical approach extends the humid area to the left edge of the panel and more accurately depicting the actual condition reported by the analysis.

[35] Figures 19–21 indicate how the TPW pattern is improved by the physical algorithm. For WV1, neither the regression nor the physical retrieval noticeably corrects the overestimate of water vapor content around 20°N, 5°W (Figure 19). This result is reasonable because of the lack of H_2O absorption bands whose weighting function profiles peak just above the surface. Figure 20 illustrates that because of the lack of H_2O absorption bands responding to the moisture parameter between 900 and 700 hPa, there are no significant improvements on the WV2 retrieval. Figure 20 demonstrates how the TPW pattern in Figure 18 is improved. The humid area near the left edge of the panel between 15°N and 20°N is missed by the forecast and is not

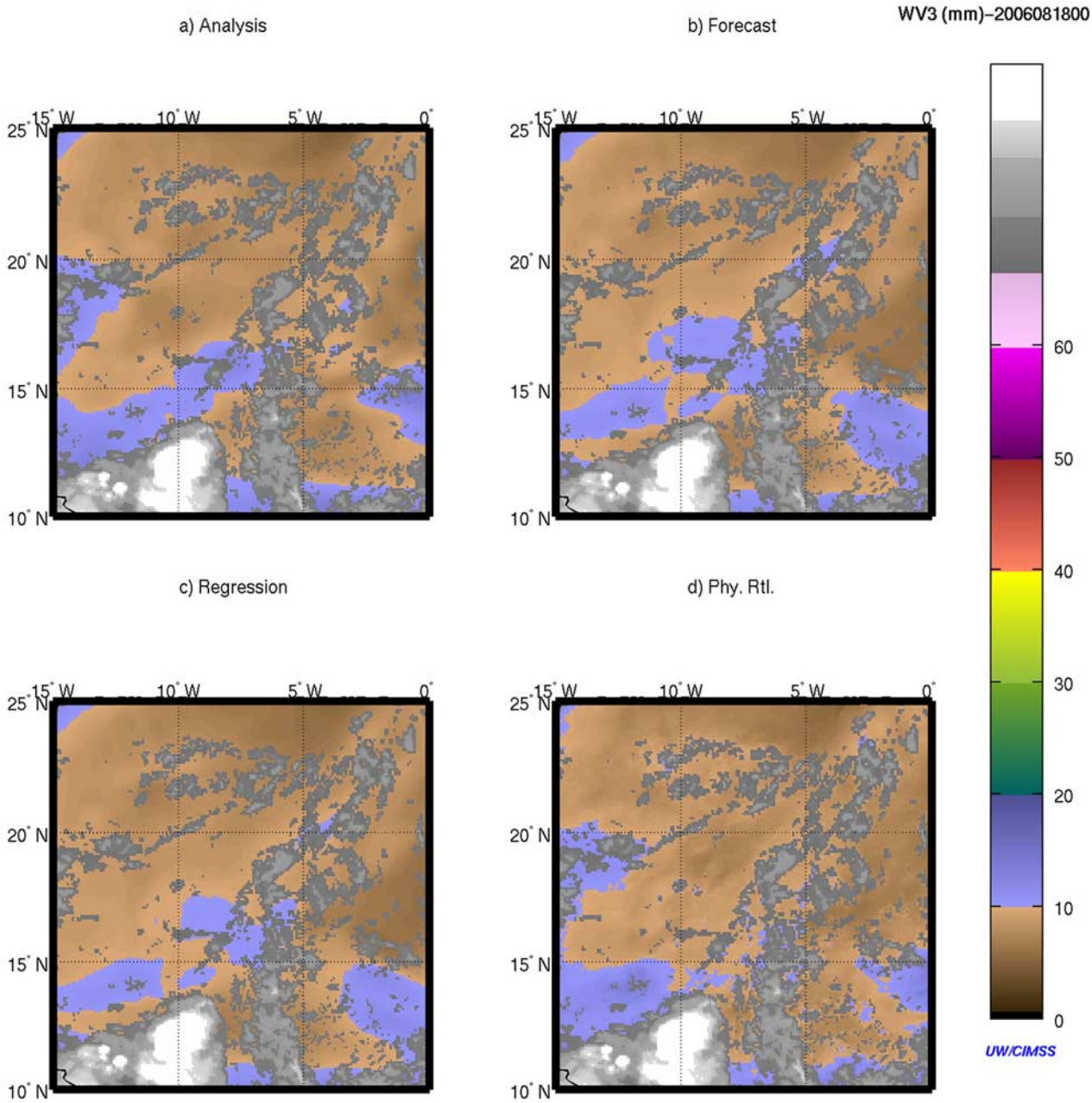

Figure 21. Same as Figure 17 but for WV3.

retrieved by the regression. Only through the physical retrieval can the humid area be retrieved.

[36] The quantitative comparisons for the full disk case at 0000 UTC on 18 August 2006 are shown in Figures 22 and 23. Only 1% of all pixels in the full disk are randomly selected for the scatterplots. In Figure 22, TPW, WV1, WV2 and WV3 are compared and in Figure 23, the LI is compared. The results from the regression are not compared here as they are worse than those from the physical retrieval. With the physical retrieval, the correlation coefficient for TPW is increased from 0.97 to 0.98 and the RMSE is reduced from 9.78% to 9.11%; for WV1, the improvement is not significant; for WV2, the correlation coefficient is increased from 0.94 to 0.95 and the RMSE is reduced by 0.5%; for WV3, the correlation coefficient is increased from 0.95 to 0.97 and the RMSE is reduced from 20.8% to 17.1%. Note that the samples selected for comparison in Figure 22 include those from both land and ocean. Because of the lack of bias adjustment for pixels over ocean, we applied the bias adjustment on radiances of pixels over land only. Further improvement on the retrievals over ocean should be possible if a reliable bias adjustment can be made. The comparison of LI shows the limitation of using SEVIRI broadband IR radiances for retrieving the temperature profiles.

5. Concluding Remarks

[37] In this paper, we discussed retrieving atmospheric profiles from SEVIRI spectral band IR radiances as a proxy

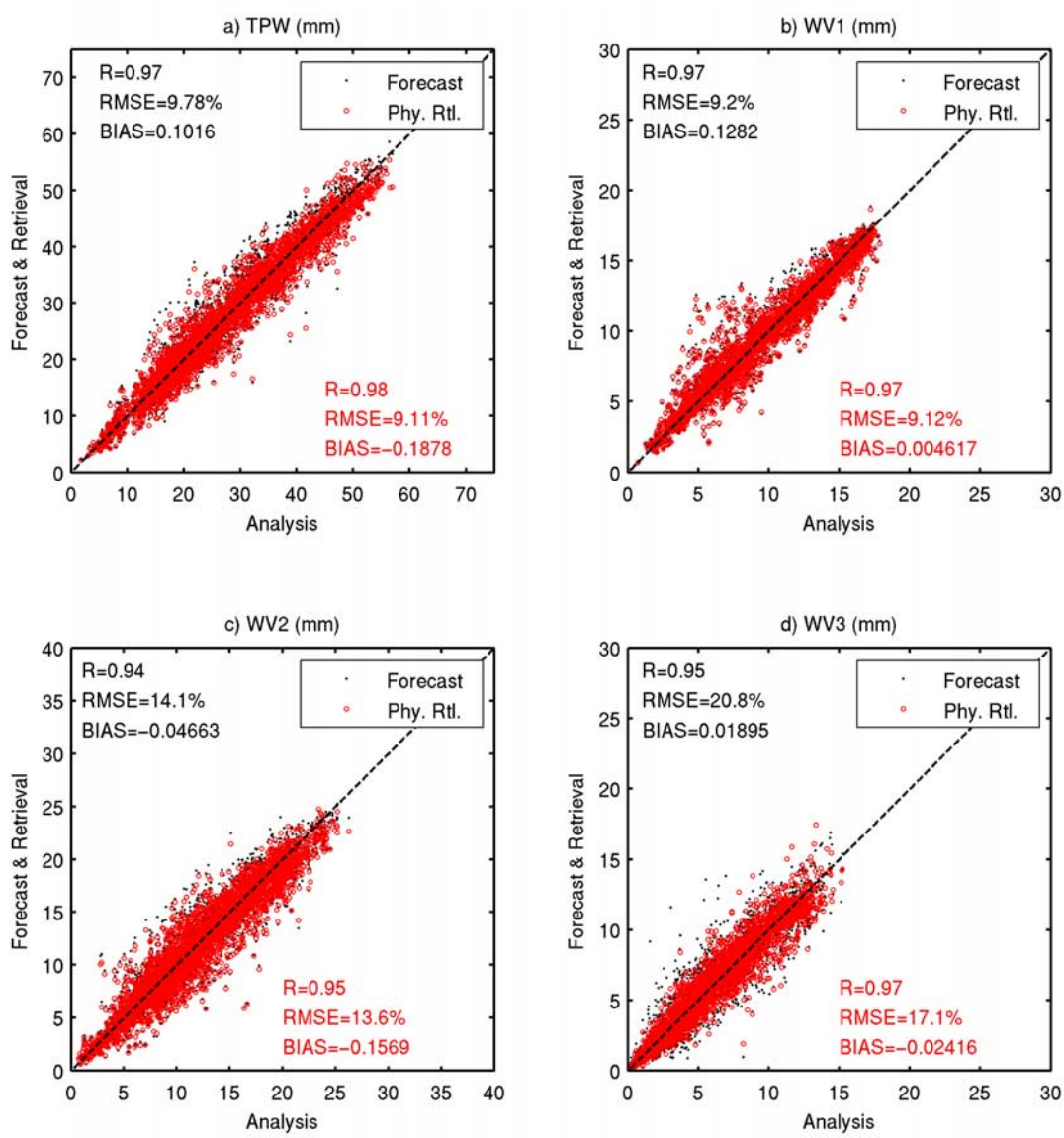

Figure 22. The scattering plots for comparing the TPW, WV1, WV2, and WV3 derived by the physical retrieval with those from forecast. The analysis data are taken as the true. The samples are randomly selected 1% of all pixels from the full disk at 1800 UTC, August 2006, and the sample number is 31044.

for ABI using the algorithm adapted from that applied to the GOES Sounder measurements. The algorithm includes a synthetic regression approach and a physical iterative retrieval approach. Both the simulation and the case study analysis prove the superiority of the physical retrieval to the forecast. Since SEVIRI/ABI only has two/three H_2O absorption bands, which correspond to the moisture variation in the upper layer (higher height than 700 hPa), the most significant improvement in water vapor profile appears in the upper layers. With only one CO_2 absorption band at 13.4/13.3 m for the temperature profile retrieval, both the numerical study and the case analysis indicate the limited temperature information from SEVIRI/ABI that can be added to the forecast.

[38] The sensitivity study indicates that for the physical retrieval, the uncertainty caused by the IR surface emissivities is small if 8.7 μm is not included in the retrieval. The emissivities from the regression or predetermined database can be used for the physical retrieval. Another numerical study shows that, relative to the emissivities, the impact of surface skin temperature uncertainty on moisture profile is relatively larger, The surface skin temperature estimate from the regression has good agreement (RMSE less than 2 K) with the truth if the temperature is limited between 250 and 310 K according to the simulation, covering most conditions for geostationary satellite remote sensing. In the physical retrieval process, surface skin temperature is simultaneously retrieved with temperature and moisture profiles.

[39] Some in situ radiosonde profiles are used as true profiles in the radiative transfer model to make a bias correction before applying the algorithm to the real data. It is proved that both water-vapor-absorbing bands have noticeable biases when comparing the calculated brightness temperatures with the SEVIRI observations. After the

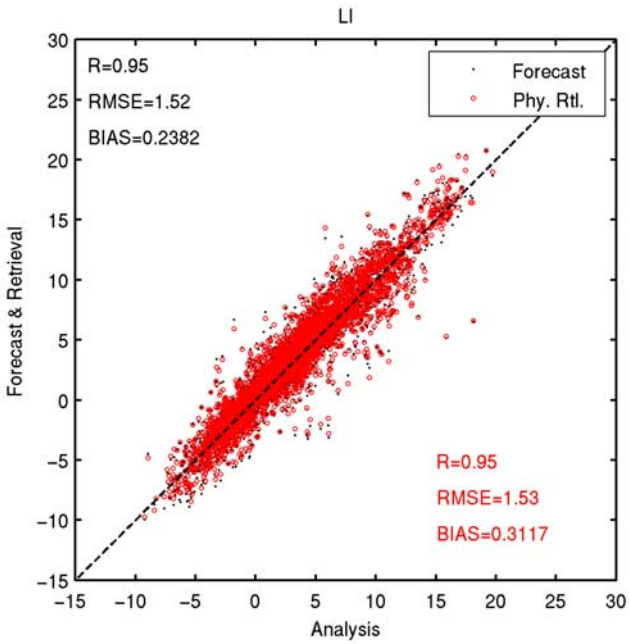

Figure 23. Same as Figure 22 but for the lifted index only.

radiance bias adjustment, the quality of water vapor profiles retrieved from the physical approach is significantly improved. A caveat in this study is that we only have in situ radiosonde profiles collected over the land. The bias adjustment may cause errors when applying the derived fitting equations to pixels over the ocean.

[40] The TPW from the physical retrieval is also compared to that from AMSR-E over ocean using a large number of samples. Relative to other similar research [*Martinez et al.*, 2007], the results are encouraging in terms of the high correlation coefficient (0.96) and small RMSE (<10%). Moreover, the SEVIRI TPW product is insensitive to surface types and does not show noticeable biases with the variation of LZA. However, the physical algorithm still underestimates TPW when the TPW is greater than 25 mm and overestimates it when TPW is less than 25 mm, similar to the performance of MODIS in retrieving TPW with a similar algorithm [*Seemann et al.*, 2003]. This issue needs further investigation.

[41] According to this study, useful water vapor information, especially the upper level moisture information, at high temporal/spatial resolution from geostationary satellite-based instruments such as SEVIRI and ABI, can be derived. Since ABI and SEVIRI are not sounder instruments, the water vapor products provided by SEVIRI/ABI are preferred to those vertically integrated parameters, instead of the profile.

[42] **Acknowledgments.** This study was partially supported by NOAA NESDIS GOES-R grant (NA06NES4400002) as part of the Algorithm Working Group (AWG). The authors would like to thank Zhenglong Li for discussion and help on this study. SEVIRI data were provided by EUMETSAT. Miguel Angel Martrinez and Marcelino Manso at the EUMETSAT nowcasting SAF (Satellite Application Facility) are thanked for the collaboration on using SEVIRI and ECMWF data for algorithm development. The views, opinions, and findings contained in this report are those of the authors and should not be construed as an official National Oceanic and Atmospheric Administration or U.S. Government position, policy, or decision.

References

Aires, F., W. B. Rossow, N. A. Scott, and A. Chédin (2002), Remote sensing from the infrared atmospheric sounding interferometer instrument: 2. Simultaneous retrieval of temperature, water vapor, and ozone atmospheric profiles, *J. Geophys. Res.*, *107*(D22), 4620, doi:10.1029/2001JD001591.

Aminou, D. et al. (2003), Meteosat Second Generation: A comparison of on-ground and on-flight imaging and radiometric performances of SEVIRI on MSG-1, paper presented at Meteorological Satellite Conference, Eur. Organ. for the Exploit. of Meteorol. Satell. Weimar, Germany, 29 Sept . to 3 Oct .

Chahine, M. T., et al. (2006), AIRS: Improving weather forecasting and providing new data on greenhouse gases, *Bull. Am. Meteorol. Soc.*, *87*, 911–926.

Eyre, J. R., and H. M. Woolf (1988), Transmittance of atmospheric gases in the microwave region: A fast model, *Appl. Opt.*, *25*, 3244–3249.

Fetzer, E. J., B. H. Lambrigtsen, A. Eldering, H. H. Aumann, and M. T. Chahine (2006), Biases in total precipitable water vapor climatologies from Atmospheric Infrared Sounder and Advanced Microwave Scanning Radiometer, *J. Geophys. Res.*, *111*, D09S16, doi:10.1029/2005JD006598.

Hannon, S., L. L. Strow, and W. W. McMillan (1996), Atmospheric infrared fast transmittance models: A comparison of two approaches, *Proc. SPIE Int. Soc. Opt. Eng.*, *2830*, 94–105.

Köpken, C., G. Kelly, and J.-N. Thépaut (2004), Assimilation of Meteosat radiance data within the 4D-Var system at ECMWF: Assimilation experiments and forecast impact, *Q. J. R. Meteorol. Soc.*, *130*, 2277–2292, doi:10.1256/qj.02.230.

Li, J. (1994), Temperature and water vapor weighting functions from radiative transfer equation with surface emissivity and solar reflectivity, *Adv. Atmos. Sci.*, *11*, 421–426, doi:10.1007/BF02658162.

Li, J., and H.-L. Huang (1999), Retrieval of atmospheric profiles from satellite sounder measurements by use of the discrepancy principle, *Appl. Opt.*, *38*(6), 916–923, doi:10.1364/AO.38.000916.

Li, J., W. Wolf, W. P. Menzel, W. Zhang, H.-L. Huang, and T. H. Achtor (2000), Global soundings of the atmosphere from ATOVS measurements: The algorithm and validation, *J. Appl. Meteorol.*, *39*, 1248–1268, doi:10.1175/1520-0450(2000)039<1248:GSOTAF>2.0.CO;2.

Li, Z., J. Li, W. P. Menzel, T. J. Schmit, J. P. Nelson III, J. Daniels, and S. A. Ackerman (2008), GOES sounding improvement and applications to severe storm nowcasting, *Geophys. Res. Lett.*, *35*, L03806, doi:10.1029/2007GL032797.

Ma, X. L., T. Schmit, and W. L. Smith (1999), A non-linear physical retrieval algorithm—Its application to the GOES-8/9 sounder, *J. Appl. Meteorol.*, *38*, 501–513, doi:10.1175/1520-0450(1999)038<0501:ANPRAI>2.0.CO;2.

Martinez, M. A., M. Velazquez, M. Manso, and I. Mas (2007), Application of LPW and SAI SAFNWC/MSG satellite products in pre-convective environments, *Atmos. Res.*, *83*, 366–379, doi:10.1016/j.atmosres.2005.10.022.

Menzel, W. P., and J. F. W. Purdom (1994), Introducing GOES-I: The first of a new generation of Geostationary Operational Environmental Satellites, *Bull. Am. Meteorol. Soc.*, *75*, 757–781, doi:10.1175/1520-0477(1994)075<0757:IGITFO>2.0.CO;2.

Menzel, W. P., F. C. Holt, T. J. Schmit, R. M. Aune, T. J. Schreiner, G. S. Wade, and D. Gray (1998), Application of GOES-8/9 soundings to weather forecasting and nowcasting, *Bull. Am. Meteorol. Soc.*, *79*, 2059–2077, doi:10.1175/1520-0477(1998)079<2059:AOGSTW>2.0.CO;2.

Rodgers, C. D. (1976), Retrieval of atmospheric temperature and composition from remote measurements of thermal radiation, *Rev. Geophys.*, *14*, 609–624, doi:10.1029/RG014i004p00609.

Rothman, L. S., et al. (1998), The HITRAN molecular spectroscopic database and HAWKS (HITRAN Atmospheric Workstation), *J. Quant. Spectrosc. Radiat. Transfer*, *60*, 665–710, doi:10.1016/S0022-4073(98)00078-8.

Schmetz, J., P. Pili, S. Tjemkes, D. Just, J. Kerkmann, S. Rota, and A. Ratier (2002), An introduction to Meteosat Second Generation (MSG), *Bull. Am. Meteorol. Soc.*, *83*, 977–992, doi:10.1175/1520-0477(2002)083<0977:AITMSG>2.3.CO;2.

Schmit, T. J., W. F. Feltz, W. P. Menzel, J. Jung, A. P. Noel, J. N. Heil, J. P. Nelson, and I. I. I. Wade (2002), Validation and use of GOES sounder moisture information, *Weather Forecast.*, *17*, 139–154, doi:10.1175/1520-0434(2002)017<0139:VAUOGS>2.0.CO;2.

Schmit, T. J., M. M. Gunshor, W. Paul Menzel, J. Gurka, J. Li, and S. Bachmeier (2005), Introducing the next-generation advanced baseline imager (ABI) on GOES-R, *Bull. Am. Meteorol. Soc.*, *86*, 1079–1096, doi:10.1175/BAMS-86-8-1079.

Schmit, T. J., J. Li, J. J. Gurka, M. D. Goldberg, K. J. Schrab, J. Li, and W. F. Feltz (2008), The GOES-R ABI (Advanced Baseline Imager) and the continuation of current sounder products, *J. Appl. Meteorol. Climatol.*, doi:10.1175/2008JAMC18581, in press.

Seemann, S. W., J. Li, W. Paul Menzel, and L. E. Gumley (2003), Operational retrieval of atmospheric temperature, moisture, and ozone from MODIS infrared radiances, *J. Appl. Meteorol.*, *42*, 1072–1091, doi:10.1175/1520-0450(2003)042<1072:OROATM>2.0.CO;2.

Seemann, S. W., E. E. Borbas, R. O. Knuteson, G. R. Stephenson, and H.-L. Huang (2008), Development of a global infrared land surface emissivity database for application to clear sky sounding retrievals from multi-spectral satellite radiance measurements, *J. Appl. Meteorol. Climatol.*, *47*, 108–123, doi:10.1175/2007JAMC1590.1.

Smith, W. L., and H. M. Woolf (1976), The use of eigenvectors of statistical covariance matrices for interpreting satellite sounding radiometer observations, *J. Atmos. Sci.*, *33*, 1127–1140, doi:10.1175/1520-0469(1976)033<1127:TUOEOS>2.0.CO;2.

Szyndel, M. D. E., G. Kelly, and J. N. Thépaut (2005), Evaluation of potential benefit of assimilation of SEVIRI water vapour radiance data from Meteosat-8 into global numerical weather prediction analyses, *Atmos. Sci. Lett.*, *6*(2), 105–111, doi:10.1002/asl.98.

Zhou, D. K., W. L. Smith, J. Li, G. W. Cantwell, A. M. Larar, J. J.-Tsou, and S. Mango (2002), Thermodynamic product retrieval methodology and validation for NAST-I, *Appl. Opt.*, *41*, 6957–6967, doi:10.1364/AO.41.006957.

M. D. Goldberg and T. J. Schmit, Center for Satellite Applications and Research, NESDIS, NOAA, Camp Springs, MD 20746, USA.

J. J. Gurka, GOES-R Program Office, OSD, NESDIS, NOAA, 5200 Auth Road, FB-4, Room 3010B, Camp Springs, MD 20746, USA.

X. Jin, J. Li, and J. Li, Cooperative Institute for Meteorological Satellite Studies, University of Wisconsin–Madison, 1225 West Dayton Street, Madison, WI 53706, USA. (xjin@ssec.wisc.edu)